Increasing the diameter of vertically aligned, hexagonally ordered pores in mesoporous silica thin films

Nabil A. N. Mohamed,[a] Yisong Han,[b] Andrew L. Hector,[a]* Anthony R. Houghton,[c] Elwin Hunter-Sellars,[c] Gillian Reid,[a] Daryl R. Williams[c] and Wenjian Zhang[a]

[a] School of Chemistry, University of Southampton, Highfield, Southampton SO17 1BJ, UK. Email A.L.Hector@soton.ac.uk

[b] Department of Physics, University of Warwick, Coventry CV4 7AL, UK

[c] Department of Chemical Engineering, Imperial College London SW7 2AZ, UK

Abstract
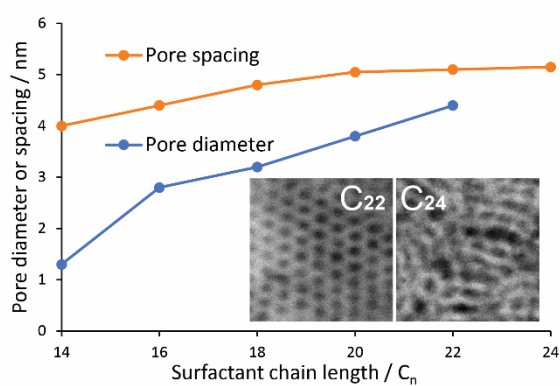
The variation in pore size in mesoporous films produced by electrochemically assisted surfactant assembly (EASA) with surfactant chain length is described. EASA produces a hexagonal array of pores perpendicular to the substrate surface by using an applied potential to organize cationic surfactants and the resultant current to drive condensation in a silica sol. Here we show that a range of pore sizes between 2 and 5 nm diameter is available with surfactants of the form $[Me_3NC_nH_{2n+1}]Br$, with alkyl chain lengths between C_{14} and C_{24}. Film quality, pore order, pore size and pore accessibility are probed with a range of techniques.

Introduction

Oriented mesoporous silica films are potential hard templates for the electrodeposition of nanowire-based devices,[1] with possible applications in Li-ion batteries[2,3], thermoelectrics[4] and supercapacitors.[5] In order for the electrode surface to remain accessible to the electrolyte it is necessary to arrange the pores perpendicular to the substrate surface, often referred to as the vertical orientation. Whilst the growth of platinum nanowires in silica with horizontal pores occurred readily, Kanno *et al*[6] showed that the electrodeposition of Au nanowires was much easier in perpendicular pores.[7] Whilst the literature on electrodeposition in very small pore templates is limited, there are some examples, e.g. of 3 nm Sn nanowires[8] or 5 to 8 nm bismuth nanowires,[9] produced in this way.

Pore orientation, pore diameter and organo-functionalization[10,11] are important factors in the rate of ion diffusion through porous films. Etienne and co-workers reported TiO_2 with the anatase structure

1

in an open porous network, in which positively charged species were more mobile than negatively charged ones.[12] The fine tuning of parameters has made silica films attractive materials for biosensing and electrochemical sensing applications,[13,14] for example Nasir et al[15] developed an electrochemical pathway for detecting cationic paraquat salts in oriented mesoporous silica films.

The most common approach to prepare mesoporous silica films is by evaporation induced self-assembly (EISA).[16,17,18] This method involves the preparation of an aqueous ethanol solution containing a surfactant and silica precursors to produce a homogenous solution of stable species. The initial surfactant concentration of the prepared solution is significantly lower in comparison to the critical micelle concentration (C_o<<CMC). Once the films have been deposited in solution by either dip or spin coating, the ethanol solvent evaporates from the deposited film resulting in the surfactant concentration increasing which in turn triggers the self-assembly process and micelle formation, producing well-organized porous structures in the liquid crystalline phase before condensing the silica species. EISA tends to produce ordered silica films with the pores either horizontal to the substrate surface or randomly oriented.

Several strategies have been devised to produce orientated silica films through application of a magnetic field,[19] epitaxial growth,[20] and radio sputtering.[21] For example, Yamauchi used an external magnetic field to control pore alignment from an EISA process either vertically or horizontally to the substrate surface .[22] Otomo et al.[23] synthesized aligned mesoporous silica films by a radiofrequency sputter deposition of Co-Si-O films where the surface morphology was influenced by a range of argon gas pressures followed by wet chemical etching to remove the Co fragment from the films. Stöber-solution growth is based on formation of hemispherical micelles of a cationic surfactant on a negatively charged substrate, and interactions with silica oligomers encouraging vertical growth of those micelles.[24] This method can take days to grow very thin aligned films.

Walcarius and co-workers[25] revealed that the preparation of vertically oriented mesoporous silica films was possible under electrochemical control. The mechanism for the electrochemically assisted self-assembly (EASA) of silica comprises of applying a negative potential to the substrate to be coated, while it sits in a solution containing the surfactant and silica precursors dissolved in an ethanol/water mixture. This results in the generation of hydroxide ions in solution, and the pH swings from acidic to alkaline at the electrode surface. The electric field is thought to play a pivotal role in the self-organization of the cationic surfactant into hemi-micelles and the pH change catalyzes the polycondensation of the sol, leading to mesoporous silica films with perpendicular (vertical) pore channels (2-3 nm) and uniform film thickness (150-200 nm). Mesoporous films can be obtained by the EASA method within as little as 20 seconds.

EASA was developed with a [Me$_3$NC$_{16}$H$_{33}$]Br (CTAB or C$_{16}$TAB) surfactant, and this leads to pores with a diameter of around 2 nm depending on conditions and substrate.[26] Robertson *et al* showed that mesitylene can be used as a swelling agent for CTAB-templated EASA films on TiN, causing the pore diameter to increase from 1.6 nm to 2.4 nm.[27] However, higher amounts of mesitylene resulted in a reduction in the ordering of the porosity. Larger vertically aligned pores may facilitate the use of such films as hard templates for nanowire electrodeposition and increase the range of sensing applications. Ullah et al recently showed that polyaniline nanowires with different widths could be produced in EASA silica films produced with C$_{16}$TAB or C$_{18}$TAB.[28] Herein we demonstrate that systematic increases in the pore diameter beyond 2 nm are achievable by EASA when utilizing surfactants created by further extending the single straight alkyl chain.

Experimental

Tetradecyltrimethylammonium bromide (C$_{14}$TAB, 99%), hexadecyltrimethylammonium bromide (C$_{16}$TAB, 98%) and octadecyltrimethylammonium bromide (C$_{18}$TAB, 98%) were purchased from Sigma-Aldrich. ^{1}H and ^{13}C{^{1}H} NMR data for the surfactants in D-chloroform were collected with a Bruker AVII400 spectrometer at 25 °C. Solutions for mass spectrometry were prepared by dissolving 50 μg of the surfactant in 1 ml of methanol. The surfactants were analyzed using ultrahigh performance liquid chromatography (UHPLC) coupled to a TQD mass tandem quadrupole mass spectrometer (Waters) with a TUV detector at 254 nm. The chromatography analysis was carried out on a Waters BEH C18 column (50 mm x 2.1 mm, 1.7 μm) with a flow rate of 0.6 ml/min. The mobile phase was made up of 0.2 % formic acid in an aqueous solution and 0.2 % formic acid in acetonitrile. This was followed by the recording of the mass spectrum in the positive ion electrospray ionization mode.

The synthesis of longer chain alkyltrimethylammonium bromide surfactants (**Scheme 1**) was carried out according to Scheraga *et al.*[29] The synthesis used alkyl bromides C$_n$H$_{2n+1}$Br where n is equal to 20 (5.0001 g, 13.83 mmol ≥ 97 %, Sigma Aldrich), 22 (5.0001 g, 12.84 mmol, 96 %, Santa Cruz Biotechnology) or 24 (0.8915 g, 2.14 mmol, synthesized as described below). The alkyl bromide was dissolved in ethanol (25 cm^3) and 30% trimethylamine in an ethanol solution (7.6000 g, 128.6 mmol mmol for C$_{20}$ and C$_{22}$, or 1.3000 g, 22.0 mmol for C$_{24}$, Sigma Aldrich) was added dropwise into this solution. The mixture was refluxed at 100 °C for 8 h with stirring under a dry ice condenser. The solution was then filtered and stored overnight in a freezer to precipitate the product. The crude product was filtered, and the resulting solid was recovered using a rotary evaporator then recrystallized three times from ethanol. Final yields were 4.50 g, 10.7 mmol eicosyltrimethylammonium bromide (C$_{20}$TAB, 90%, off white solid), 4.22 g, 9.4 mmol

docosyltrimethylammonium bromide (C$_{22}$TAB, 84%, white solid) and 0.78 g, 1.6 mmol

tetracosyltrimethylammonium bromide (C$_{24}$TAB, 88%, white solid).

1-Bromoeicosane

i) Ethanol, Me$_3$N   ii) reflux 8 hours, 373 K

Eicosyltrimethylammonium bromide
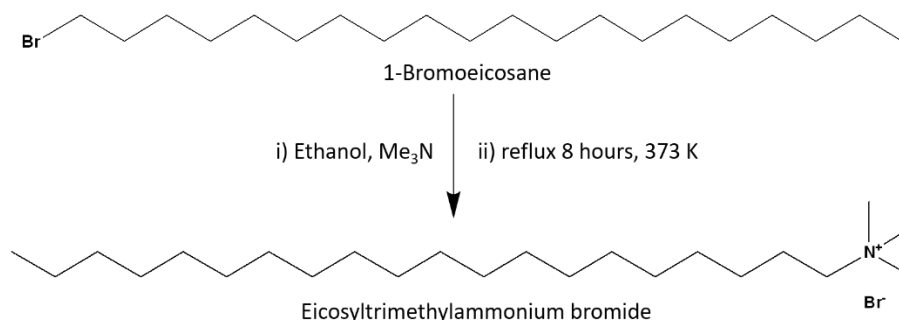
Scheme 1 Reaction of 1-bromoeicosane with trimethylamine to form the quaternary ammonium

salt, C$_{20}$TAB. The same general method was used for C$_{22}$TAB and C$_{24}$TAB surfactants.

The synthesis of 1-bromotetracosane (C$_{24}$H$_{49}$Br) was based on the procedure reported by Al-

Dulayymi *et al.*[30] The method involved dissolving triphenylphosphine (0.800 g, 3.05 mmol, 99%,

Avocado Research Chemicals Ltd), tetracosan-1-ol (1.000 g, 2.82 mmol, > 98 %, Tokyo Chemical

Industry UK Ltd) and N-bromosuccinimide (1.500 g, 8.43 mmol, 99%, Sigma Aldrich) in dry

dichloromethane (50 cm^3). The reaction mixture was stirred in a water bath at ambient temperature

for 5 hours and then quenched with water (200 cm^3), extracted into dichloromethane and dried

using a rotary evaporator to give a red solid. The product was then refluxed in petroleum ether (500

cm^3) and ethyl acetate (5 cm^3), filtered, and the filtrate dried using a rotary evaporator to give

C$_{24}$H$_{49}$Br (0.892 g, 2.14 mmol, 89.2 % yield). The material (C$_{24}$H$_{49}$Br) produced was used directly for

the preparation of the C$_{24}$TAB surfactant. NMR and mass spectra are shown in supplementary

information (Figs. S1-S9).

C$_{20}$TAB. ^{1}H NMR (CDCl$_3$): δ/ppm 0.83 (t, CH$_3$, [3H]), 1.17 (br s, CH$_2$, [32H]), 1.26-1.37 (m, CH$_2$, [2H]),

1.63-1.77 (m, CH$_2$, [2H]), 3.41 (s, CH$_3$, [9H]), 3.47-3.56 (m, CH$_2$, [2H]). ^{13}C{^{1}H} NMR (CDCl$_3$): δ/ppm

14.12, 22.70, 23.23, 26.19, 26.22, 29.23, 29.32, 29.36, 29.47, 29.54, 29.59, 29.63, 29.66, 29.68,

29.70, 29.71, 31.92, 53.41, 58.43, 67.12. MS (ESI$^+$ in CH$_3$OH): found m/z = 340.58; required for

{C$_{23}$H$_{50}$N$^+$}: m/z = 340.

C$_{22}$TAB. ^{1}H NMR (CDCl$_3$): δ/ppm 0.82 (t, CH$_3$, [3H]), 1.19 (br s, CH$_2$, [36H]), 1.29-1.37 (m, CH$_2$, [2H]),

1.61-1.65 (m, CH$_2$, [2H]), 3.41 (s, CH$_3$, [9H]), 3.47-3.53 (m, CH$_2$, [2H]). ^{13}C{^{1}H} NMR (CDCl$_3$): δ/ppm

14.10, 22.72, 23.21, 26.17, 29.22, 29.27, 29.32, 29.35, 29.36, 29.46, 29.59, 29.65, 29.66, 29.69,

29.71, 31.89, 31.91, 31.93, 42.63, 53.45, 67.18, 67.21. MS (ESI$^+$ in CH$_3$OH): found m/z = 368.60;

required for {C$_{25}$H$_{54}$N$^+$}: m/z = 368.

C$_{24}$TAB. ^{1}H NMR (CDCl$_3$) δ/ppm 0.82 (t, CH$_3$, [3H]), 1.18 (s, CH$_2$, [40H]), 1.22-1.33 (m, CH$_2$, [42H]),

1.63-1.72 (m, CH$_2$, [2H]), 3.40 (s, CH$_3$, [9H]), 3.46-3.54 (m, CH$_2$, [2H]). ^{13}C{^{1}H} NMR (CDCl$_3$): δ/ppm

14.12, 22.70, 23.25, 25.32, 25.33, 26.18, 29.20, 29.29, 29.33, 29.37, 29.44, 29.55, 29.58, 29.65, 29.67, 29.69, 29.71, 31.94, 43.65, 53.46, 53.51, 53.54, 53.59, 53.60. MS (ESI$^+$ in CH$_3$OH): found m/z = 396.70; required for {C$_{27}$H$_{58}$N$^+$}: m/z = 396.

Mesoporous silica growth

(i)   C$_{14}$TAB – C$_{18}$TAB

The synthesis of vertically ordered silica films under electrochemical control used the method previously reported by Goux *et al.*[31] The electrolyte was prepared by mixing C$_{14}$TAB (0.4801 g, 1.43 mmol), C$_{16}$TAB (0.4801 g, 1.32 mmol) or C$_{18}$TAB (0.4801 g, 1.22 mmol) into 0.1 mol dm^{-3} sodium nitrate (NaNO$_3$) in 20 cm^3 water and 20 cm^3 ethanol, then tetraethylorthosilicate (TEOS, 98%, Sigma Aldrich), 905 μL, 4.08 mmol) was added to the solution. The sol was adjusted close to pH 3 using 0.2 mol dm^{-3} HCl then allowed to hydrolyze for a duration of 2.5 hours. The ratio for the surfactant: silica precursors were kept constant at around 0.3 with each experiment containing a newly made up sol electrolyte.

(ii)   C$_{20}$TAB-C$_{24}$TAB

The sol preparation was altered slightly when using C$_{20}$TAB (0.3000 g, 0.71 mmol), C$_{22}$TAB (0.3000 g, 0.67 mmol) and C$_{24}$TAB (0.3000 g, 0.63 mmol) due to surfactant solubility problems with the standard method described above. The electrolytes were prepared by mixing 0.1 mol dm^{-3} NaNO$_3$ in water (20 cm^3) with isopropyl alcohol (20 cm^3), adding TEOS (905 μL, 4.08 mmol) and adjusting the sol pH to between 3 and 3.5 using 0.2 M HCl. The sol was then stirred for 90 minutes. The surfactants were added to the sol and allowed to stir for a further 60 minutes. The C$_{22}$TAB and C$_{24}$TAB surfactants did not dissolve in the solution at 25 °C, so the temperature was raised to 35 °C, which caused dissolution. The solutions were then allowed to hydrolyze for 2.5 hours. The surfactant: silica ratio was kept constant at around 0.17 with each experiment using a fresh sol electrolyte.

The electrodeposition process of porous silica was carried out in a Teflon cell with 2 × 1 cm indium tin oxide-coated glass (ITO; surface resistivity 8-12 Ω^{-1}, Sigma Aldrich) used as the working electrode. Prior to deposition the electrodes were washed with water and ethanol and dried under N$_2$ gas. The working electrode was submerged vertically into the sol electrolyte, a stainless-steel cone was used as the counter electrode and a silver rod was used as the reference electrode. A Biologic SP150 potentiostat was used to apply a constant potential of -1.25 V (vs. Ag/Ag$^+$) for a duration of 20 seconds. After each experiment the silica films (1 × 1 cm) were quickly rinsed with water and ethanol, then dried in an oven at 130 °C for 16 hours. To remove the surfactants from the pore channels, the films were then immersed in a solution of 0.2 mol dm^{-3} HCl (Fischer Scientific) in ethanol for 15 minutes under gentle stirring.

Film characterization

Cyclic voltammetry (CV) was used to determine the accessibility of the pores in the mesoporous silica films on ITO electrodes using a range of redox probes. The aqueous probe solution was made up of 0.5 mmol dm^{-3} ferrocene methanol (FcMeOH), 5 mmol dm^{-3} hexaammineruthenium(III) chloride ([Ru(NH$_3$)$_6$]$^{3+}$), or 0.5 mmol dm^{-3} each of potassium hexacyanoferrate(III))[Fe(CN)$_6$]$^{3-}$) and potassium hexacyanoferrate(II) trihydrate ([Fe(CN)$_6$]$^{4-}$), in all cases with 0.1 mol dm^{-3} NaNO$_3$ supporting electrolyte. The working electrode was the ITO coated with mesoporous silica, a platinum gauze was used as the counter electrode and the reference electrode contained Ag/AgCl in 4 mol dm^{-3} KCl solution. The potentiostat used was a Biologic SP150.

A Rigaku Smartlab X-ray diffractometer with a Hypix-3000 2D detector was used for grazing incidence small angle X-ray scattering (GISAXS) experiments. The incidence angle for all samples was 0.25° with measurements collected as 2D images or as 1D scans collected in-plane with 0.5° incident and 0.228° exit Soller slits and an angle range of 1-10° 2θ. Scanning electron microscopy (SEM) images were collected with a Jeol JSM-6500F operating at an accelerating voltage of 5 kV. To overcome charging, the porous silica films were coated with a thin layer of gold to improve the conductivity of the material before obtaining top view and cross-sectional scanning electron micrographs. Scanning transmission electron microscopy (STEM) images of the mesoporous silica films were recorded using a JEOL ARM200f double-corrected TEM operated at 200 kV. TEM specimens were prepared by scraping the silica films off the substrate and suspending them on lacey carbon films. The TEM specimens were tilted during the TEM observations to allow for the establishment of an edge-on condition for some silica flakes (the pores directly facing the electron beam), when the size and the arrangements of the pores are clearly revealed.

Ellipsometric porosimetry (EP) experiments were performed using a Dynamic Vapour Sorption (DVS) instrument (Surface Measurement Systems Ltd., UK) coupled with a FS-1 multi-wavelength ellipsometer (Film Sense, USA). The toluene vapor sorption experiments were carried out in an environmental chamber at a fixed temperature of 25 °C, at atmospheric pressure and a solvent partial pressure range between 0-95% P/P$_o$. The partial pressure was maintained using mass-flow controllers operating in closed-loop mode using dry air as the carrier gas with a flow rate of 100 mL/min and the partial pressure monitored using a speed of sound sensor. The ellipsometer uses four wavelengths (465, 525, 595 and 635 nm) at an angle of incidence of approximately 65°, to produce the highest possible signal intensity in the detector. The mesoporous silica films were exposed to toluene in fixed partial pressure steps ranging between 0.5-5% for 20 minutes per step to reach equilibrium, and the refractive index was continuously measured to produce isotherms.

Results and discussion

The electrochemically assisted self-assembly (EASA) method was originally devised by Walcarius[25] and has been shown to be a versatile method to produce highly ordered silica films with the pores vertical to the substrate. Previously this process has largely used C_{16}TAB as the surfactant, resulting in ~1.6 nm aligned, hexagonally ordered pores. Walcarius' group[31] studied the pore accessibility of EASA films grown with C_{12}TAB to C_{18}TAB using a FcMeOH redox probe. It was concluded that the increase in current from the CV plots was associated with increases in the lipophilic surfactant chain length.

In the present study, the deposition of silica films using a series of cationic surfactants with different alkyl chain lengths, C_{14}-C_{24}, was undertaken with the aim of producing larger pore diameters than currently available in vertical orientation.[26,32] Deposition potentials above -1.2 V (vs. Ag/Ag$^+$) result in no film formation, whereas below -1.3 V (vs. Ag/Ag$^+$) the ITO electrode is damaged by reduction of indium oxide. Depositions were carried out at -1.2 V, in the middle of the deposition window. The range at which depositions occur are between 10-20 seconds with thickness values of 40-150 nm, with lengthier deposition times resulting in loss of uniformity due to surface aggregates.[33,25] The longer alkyl chain lengths increase the hydrophobicity of the surfactant, so the sol composition and temperature had to be varied to achieve surfactant solubility and produce highly ordered porous silica films, including switching the ethanol component of the sol to isopropyl alcohol. The films were then dried and the surfactant removed by solvent extraction as described above.

Structure and characterization of mesoporous silica films

The pore ordering and alignment in mesoporous silica was determined by GISAXS measurements. The 1D in-plane scattering pattern for the EASA film grown with C_{22}TAB is shown in Fig. 1, and contains the typical peaks for mesoporous materials with a hexagonal arrangement of cylindrical pores in *P6mm* symmetry, namely the SBA-15[34,35] and MCM[36,37] families of materials. The incident beam angle found to provide the most intense diffraction features was 0.25°, and the 10, 11, 20 and 21 peaks were observed at 2.00°, 3.43°, 3.96° and 5.22°. As calculated from eq (1) and eq (2), the 10 peak position corresponds to a d-spacing of 4.42 nm and the resulting pore spacing/lattice parameter, a_H is 5.10 nm for the silica film with C_{22}TAB. The same set of peaks was also observed for films produced with the surfactants from C_{14}-C_{20}.

$$d_{10} = \frac{\lambda}{2sin\theta} \qquad \text{Eq 1}$$

$$a_H = \frac{d_{10}}{\cos 30} \qquad \text{Eq 2}$$

In contrast, the addition of $C_{24}TAB$ to the sol electrolyte resulted in a disordered sol-gel film as indicated by the 1D in-plane GISAXS data shown in Fig. 1. A clear reduction in the intensity of the broad 10 diffraction peak and a total loss of the 11 and 20 diffraction peaks was observed, indicating a significant loss of the hexagonal order. $C_{22}TAB$ is the maximum chain length with which we could obtain ordered porosity and thus this approach allows an expansion in the pore spacing of ordered films up to 5.10 nm.
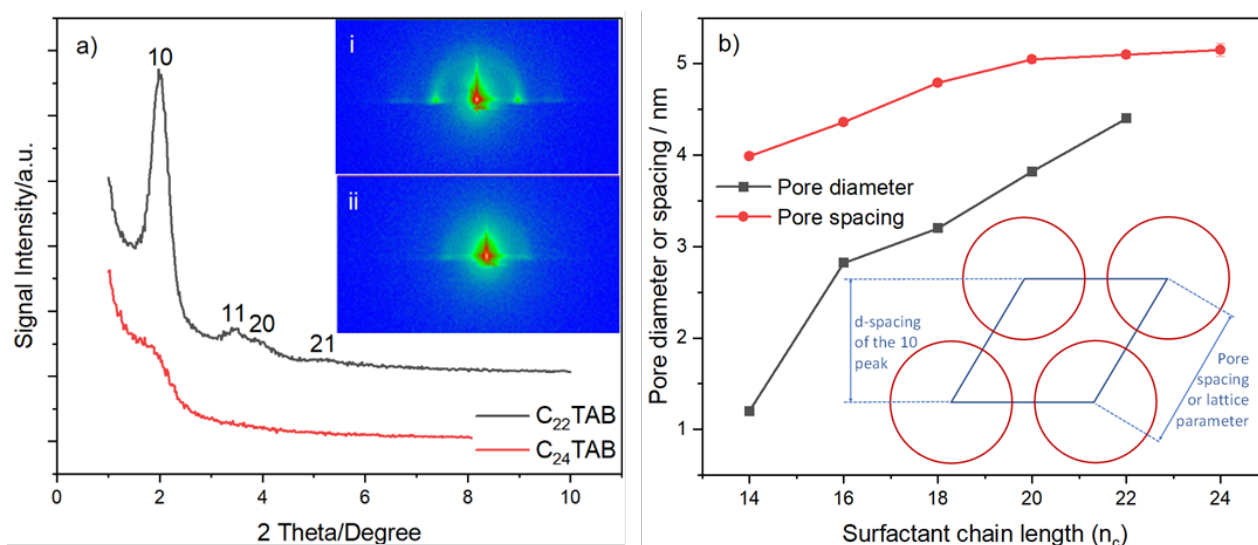
Figure 1. (a) 1D in-plane GISAXS patterns of EASA films with $C_{22}TAB$ and $C_{24}TAB$ deposited at a potential of -1. 25 V (vs. Ag/Ag$^+$) for 20 s on ITO electrodes (inset: 2D GISAXS patterns for (i) $C_{22}TAB$ and (ii) $C_{24}TAB$ templated EASA films) and (b) a plot of pore spacing (nm) of the 10 reflection and pore diameter (nm) determined by ellipsometric porosimetry as a function of surfactant chain lengths of EASA films grown with $C_{14}TAB$[32], $C_{16}TAB$, $C_{18}TAB$, $C_{20}TAB$, $C_{22}TAB$ and $C_{24}TAB$. Further GISAXS data are given in supplementary information (Figs. S10-S13).

The 2D GISAXS image of the EASA film templated with $C_{22}TAB$ is presented in the insets to Fig. 1(i). The four in-plane spots in the horizontal plane relate to the 10, 11, 20 and 21 reflections discussed in the previous paragraph. The position of these spots in the horizontal plane shows that the pores are oriented vertically, i.e. perpendicular to the plane of the substrate. Out-of-plane rings of low intensity are also observed at similar d-spacings to the in-plane spots, and these features increase in intensity with longer deposition times. Goux *et al*[31] reported similar GISAXS features for $C_{16}TAB$-generated EASA films, due to the growth of silica spheres at the surface with random alignment of the hexagonal pores. The second inset to Fig. 1(ii) illustrates the 2D GISAXS data obtained for the EASA film templated with $C_{24}TAB$ after surfactant removal. The position of the 10 diffraction spots in

the horizontal plane shows this film also has vertically aligned pores, but the hexagonal domains have very little longer-range order, which also accounts for the low intensity of the 1D GISAXS pattern.

The pore spacings as a function of surfactant chain length (C_{14}, C_{16}, C_{18}, C_{20}, C_{22} and C_{24}) for a range of EASA films are also shown in Fig. 1. An increase in the pore spacing values upon increasing the surfactant size is observed. This indicates a likely expansion of the pores, but does not account for the thickness of the pore walls and hence is not a direct measure of changing pore diameter. The pore spacing values start to plateau at longer chain lengths (C_{22} and C_{24}), suggesting that the effect on pore diameter is reaching a limit using these linear chain surfactants.

The silica films were soaked in a solution containing 0.2 mol dm^{-3} HCl in ethanol to remove the surfactant from the films. Top view SEM images (Fig. 2) provided evidence that the film was free of microcracks. The coating thickness of mesoporous silica was found through cross-sectional imaging to be in the range of 100-150 nm, similar to films produced with C_{16}TAB under similar conditions.[25] The presence of silica aggregates on the electrode surface arises from the diffusion of hydroxide ions from the electrode-electrolyte interface and into the neighboring bulk solution.[38] The diffusion layer thickness was calculated by $\sqrt{\pi D T}$ (where D is the diffusion coefficient in which OH$^-$ equals to 4x10^{-5} cm^2 s^{-1} and t is the time taken for the deposition process) is notably larger (500 μm) than the thickness of the aligned porous silica films. In this diffusion layer, silica continues to condense in the bulk solution resulting in a layer of silica sphere aggregates on the film's surface produced through a conventional Stöber process,[24,38] also visible in Fig. 2. This silica overgrowth can be removed with sticky tape (supplementary information, Fig S14), or reduced by either optimizing the sol composition, or adjusting the deposition potential and time. The "Scotch tape test" can also be used to test film adhesion on the ITO surface, and when tape is attached directly onto the surface and peeled off the silica remains intact.
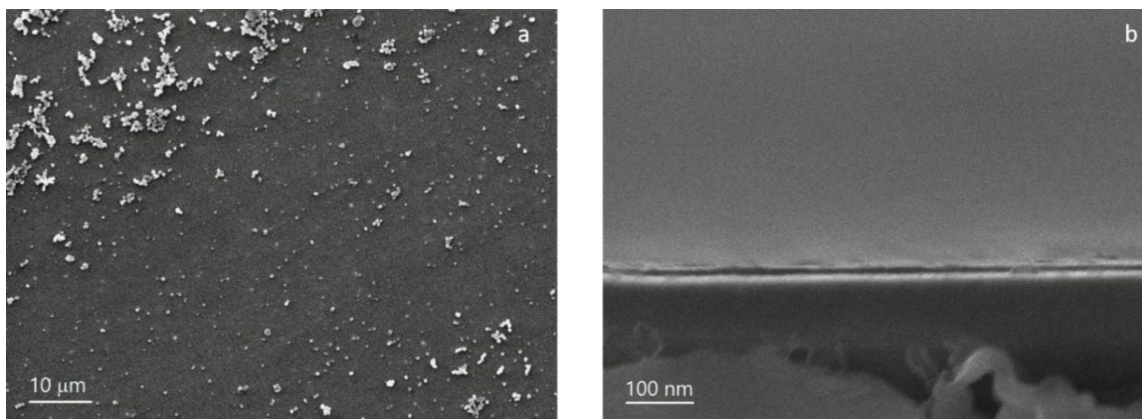
Figure 2. (a) Top view and (b) cross-sectional SEM image of a C_{18}TAB-templated film deposited at an applied potential of -1.25 V (Ag/Ag$^+$) for 20 s on an ITO electrode.

To further investigate the porous silica structure, TEM samples were prepared using EASA films prepared from C_{22}TAB and C_{24}TAB. The GISAXS data (Fig. 1) had suggested the strong hexagonal order found with C_{16}TAB could be maintained to C_{22}TAB, but that with C_{24}TAB loss of order had occurred. The images in Fig. 3 support this finding, since the mesopores in the C_{22}TAB-derived silica film have vertical orientation with large hexagonal domains across the film. In contrast, the TEM samples of silica films prepared with C_{24}TAB retain the mesoporosity but have only very small regions of hexagonal order in the pore structure. This image was taken through a flake of silica removed from the film with a scalpel which sits flat on the TEM grid, and the pores are clearly still vertical, consistent with the GISAXS data.
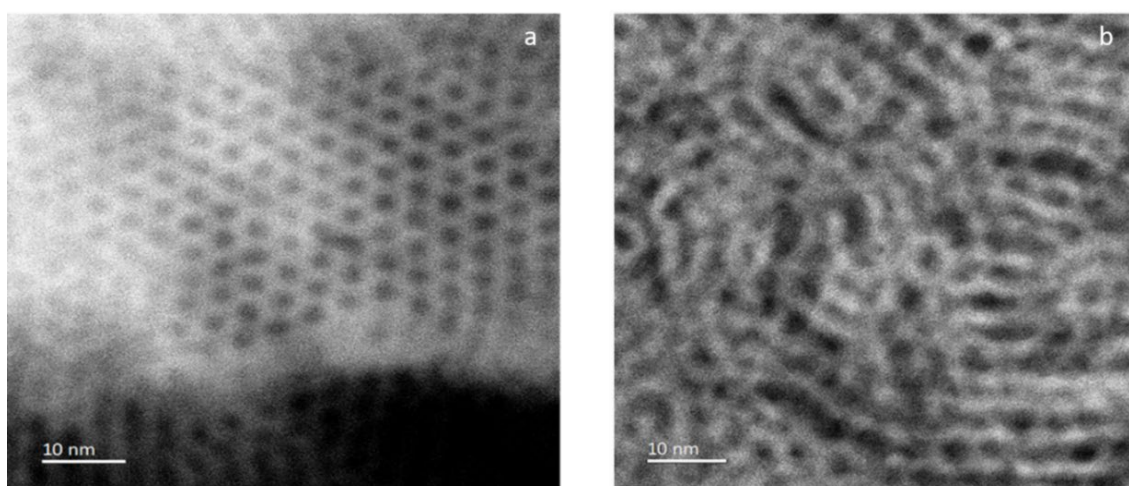

Figure 3. TEM images of mesoporous silica films produced with (a) C_{22}TAB and (b) C_{24}TAB deposited at -1.25 V (vs. Ag/Ag$^+$) for 20 s on ITO electrodes.

Ellipsometric porosimetry

Ellipsometric porosimetry (EP) was used to examine the silica surface of EASA films grown with different sized surfactants. EP can provide detailed information about the porosity, sorption isotherms and pore size distribution. Toluene was chosen as the probe molecule as it primarily interacts with surfaces through non-polar dispersion forces.[39,40] Highly polar solvents such as water are likely to produce large hysteresis because of interaction with the hydroxyl groups on the pore wall during the adsorption/desorption process.[41] Changes in refractive index values were measured during the experiment, which allowed for the volume fraction of toluene present within the pores to be calculated using the Lorentz-Lorenz effective medium approximation.[39]

In Fig. 4a (inset) the silica films containing $C_{16}TAB$ generated an isotherm with characteristics of Type I (b) and Type IV (b)[42], with a very minor step noticed at around 0.09 P/P_0, when exposed to toluene vapor. The initial increase in volume fraction up to 0.17 P/P_0 is in line with mixed monolayer-multilayer formation on the surface of the material and large micropore or small mesopore filling, of which the latter is most likely dominant. The isotherm, unlike typical Type I (b) and Type IV (b) shapes, does not fully plateau after the inflection point at P/P_0 = 0.17, almost like a Type II isotherm. This indicates that some degree of heterogeneous mesoporosity is present, which is supported by the gradual decrease in pore volume as pore diameter increases past 4-5 nm and is also present in all the other films. The adsorption-desorption branches present minimal hysteresis, likely due to the size of the mesopores within the material being below the critical diameter for capillary condensation to occur. In comparison, nitrogen systems at -196 °C show hysteresis in pores wider than ~4 nm,[42] although the critical diameter for toluene vapor at ambient conditions has not been determined quantitatively.
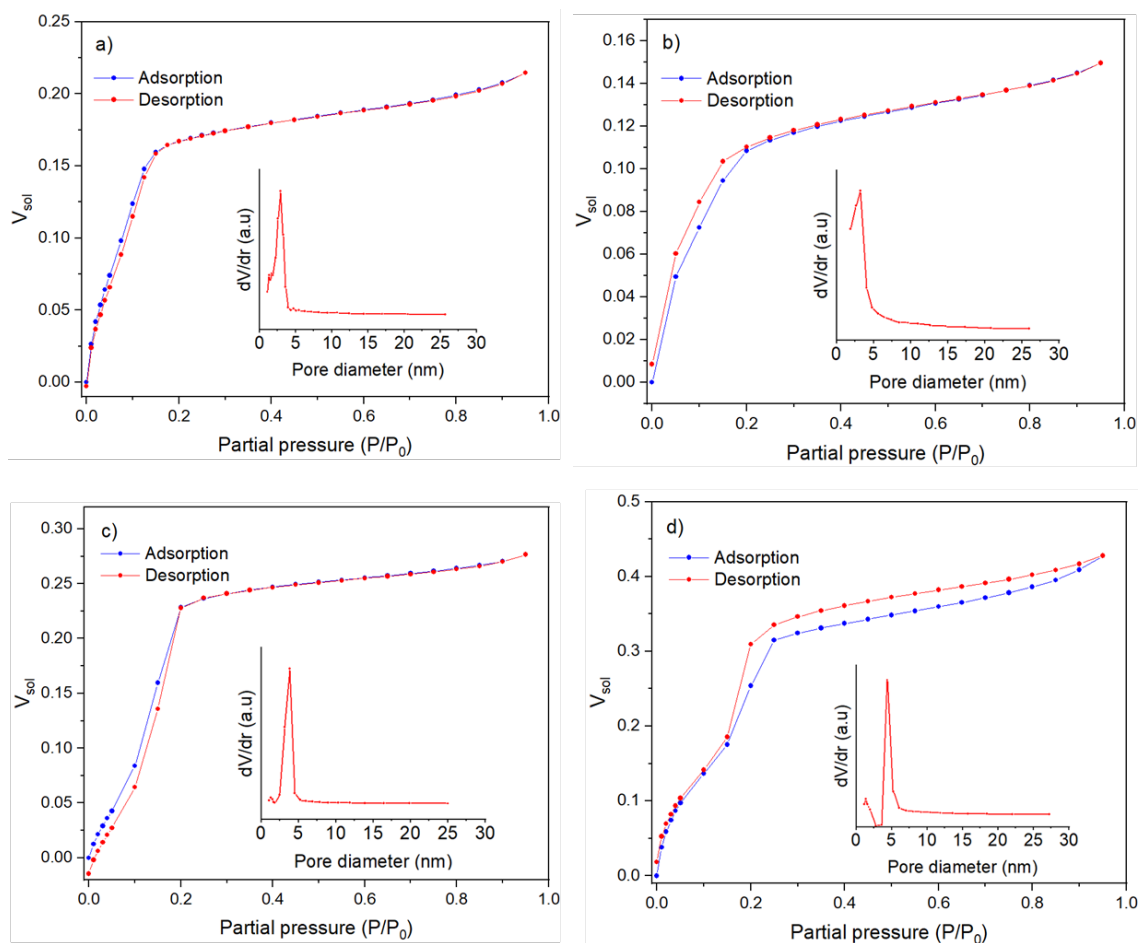
Figure 4. The adsorption/desorption isotherms of the EASA films grown with (a) C_{16}TAB, (b) C_{18}TAB, (c) C_{20}TAB and (d) C_{22}TAB surfactants using toluene. The insets show the corresponding pore size distributions.

Films made with C_{18} (Fig. 4b inset) also produced an isotherm with similar characteristics to C_{16} with the step around 0.10 P/P_0 still observed. The curvature at which the uptake levels off is broader than in the film produced with the C_{16} surfactant, a result that can be attributed to a greater degree of heterogeneous mesoporosity for this particular sample. There is a low level of hysteresis present in the low partial pressure region of 0-0.2 P/P_0, and the solvent volume fraction does not return to zero after desorption, likely due to some small quantity of toluene remaining trapped within the material. A common reason for this to occur is that the material contains micropores or narrow pore constrictions, in this case with size similar to that of the kinetic diameter of toluene (0.585 nm).[43] Micropores are common in sol-gel derived materials due to the formation of the polymer network in solution.[44] No hysteresis was present at medium to high partial pressures, again suggesting that any mesopores present have a size below the critical hysteresis diameter.

The silica film grown with C_{20}TAB (Fig. 4c inset) exhibited similar isotherm characteristics as C_{16} and C_{18}, however was found to possess a more noticeable, sharper step around 0.10 P/P_0, as is associated

with Type IV isotherms. The sharper step implies that the transition from surface adsorption to pore filling is more distinct and points to C_{20} having narrower PSD compared to C_{16} and C_{18}, as seen in the PSD plot. This phenomenon is common in ordered mesoporous silicas, with a study by Calleja *et al* [45] observing a similar isotherm shape for MCM-41 exposed to nitrogen, although the transition from surface to pore filling was observed to occur at a partial pressure between 0.15-0.2 P/P_0. There was also still no hysteresis observed at higher partial pressures in the isotherm.
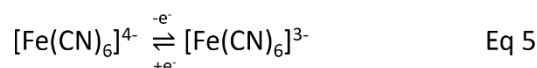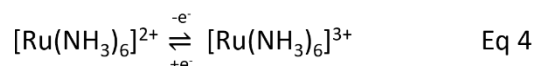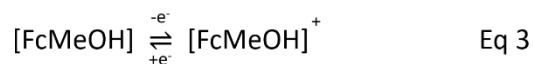
For the film with C_{22}TAB, the shape of the isotherm matches closest to that of a Type IV (a), which is common for mesoporous materials. The step in the isotherm has shifted towards a higher partial pressure of around 0.15 P/P_0, although still lower than that of typical Type IV (a) isotherms. It also presents hysteresis, which suggests the critical mesopore diameter has been reached and capillary condensation occurs. Both these observations are consequences of an increase in pore size. The hysteresis loop most closely matches the H4 and H5 type, which have been associated with micro-mesoporous carbons and templated silicas, respectively.[42]

Fig. 4 also shows the pore size distribution (PSD) curves for the silica films with increasing chain lengths, C_{16}-C_{22}, which were calculated according to the modified Kelvin equation where the pores are assumed to have cylindrical symmetry[34]. These plots display peak pore sizes in the region of 2.82, 3.24, 3.82 and 4.40 nm for the surfactants of C_{16}-C_{22}, respectively, which were all obtained from the desorption branch of the isotherms. The sharp peaks observed in the PSD plots are indicative of a high level of homogeneous pore size and porosity in the ordered mesoporous silica materials. Interestingly, it is also noticed that the pore diameter increases steadily upon increasing the carbon units in the surfactant chain. This compared well with the GISAXS-derived pore spacing in Fig. 1, and shows a fairly consistent trend.

Electrochemical characterization of the films

The pore accessibilities of the mesoporous silica films on ITO electrodes were investigated using a range of redox active probes: 0.5 mmol dm^{-3} [FcMeOH], 5 mmol dm^{-3} [Ru(NH$_3$)$_6$]$^{3+/2+}$or 0.5 mmol dm^{-3} [Fe(CN)$_6$]$^{3-/4-}$ in solutions also containing 0.1 mol dm^{-3} NaNO$_3$ as the supporting electrolyte. This approach has been used previously to demonstrate pore accessibility in EASA-derived silica films,[25,46] with similar results to those shown in the supplementary information for films made with C_{18}TAB, C_{20}TAB and C_{22}TAB (Figs. S15-S17). The reversible redox reactions of the active species are shown in Eq 3-5. In brief, the as-prepared silica films containing surfactant have a strong suppression of the electrochemical current with the charged probes, showing the films to have good coverage. A smaller reduction in current and a positive shift in the oxidation/reduction potentials with ferrocene methanol is due to this probe's solubility in the surfactant and interaction with it. After surfactant removal, the peak potential separations and the currents were similar to those observed on bare ITO

with the ferrocene methanol and ruthenium hexamine probes. This suggests a high degree of pore accessibility. In the case of the hexacyanoferrate probe, somewhat lower currents and a larger peak separation with the mesoporous silica films are associated with the interaction between the negatively charged silica walls and the probe, i.e. the Gibbs-Donnan effect.[46,47]

$$[FcMeOH] \underset{+e^-}{\overset{-e^-}{\rightleftharpoons}} [FcMeOH]^+ \qquad \text{Eq 3}$$

$$[Ru(NH_3)_6]^{2+} \underset{+e^-}{\overset{-e^-}{\rightleftharpoons}} [Ru(NH_3)_6]^{3+} \qquad \text{Eq 4}$$

$$[Fe(CN)_6]^{4-} \underset{+e^-}{\overset{-e^-}{\rightleftharpoons}} [Fe(CN)_6]^{3-} \qquad \text{Eq 5}$$

It is evident that extending the alkyl chain length of surfactants (C_{14}, C_{16}, C_{18}, C_{20} and C_{22}) affects the rate of diffusion of the active species into the porous silica medium.

Figure 5 shows CVs recorded with a film produced from C_{22}TAB (others in supplementary information, Figs. S18-S21) at scan rates between 2 and 100 mV s^{-1} for [FcMeOH] and $[Ru(NH_3)_6]^{3+/2+}$ and between 2 and 20 mV s^{-1} for $[Fe(CN)_6]^{4-/3-}$. The CV profiles became distorted at faster scan rates than this for the anionic species. The peak potential (I_p) as a function of the square root of scan rate ($v^{1/2}$) is shown in Figs. 5d-f. A linear trend is observed for I_p vs $v^{1/2}$ scan rate, suggesting that the current is governed mainly by diffusion.

For electron transfer reactions of diffusional processes in solution, it is possible to use the Randles-Sevcik (RS) equation to determine the diffusion coefficients of redox active species through the porous silica medium. The RS equation (Eq 6) describes how the current increases exponentially with the square root of scan rate. I_p is the peak current, n is the number of electrons transferred in the oxidation and reduction reaction, A is the electrode area, D is the diffusion coefficient, T is the temperature and C is the concentration of the bulk solution. In the CV plots, the peak potential separations are greater than 59 mV for the various redox active species, indicating effects due to iR drop and possible quasi-reversible behavior. The RS equation applies to electrochemically reversible systems, so the calculated diffusion coefficients will be affected by resistance effects. The shift in peak current position with scan rate is likely due to iR drop. In Fig. 5b, the increase in concentration of the ruthenium species results in a dramatic increase in current in comparison to the lower concentrations of FcMeOH and $[Fe(CN)_6]^{4-/3-}$species, indicating a greater iR drop.

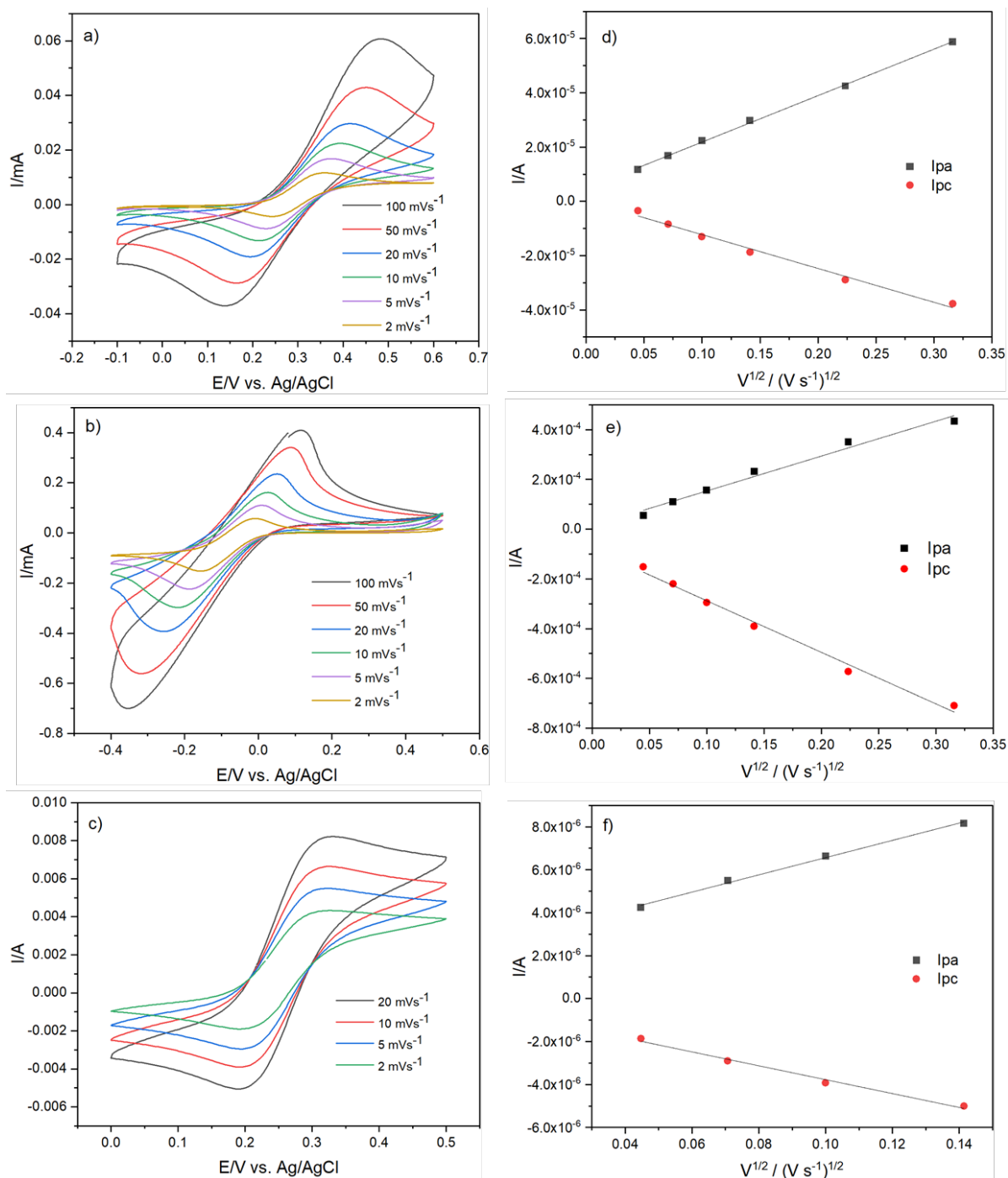$$i_p = (2.69 \times 10^5)\ n^{3/2}ACD^{1/2}v^{1/2} \qquad \text{Eq 6}$$

Figure 5. The CVs of (a) 0.5 mmol dm^{-3} [FcMeOH], (b) 5 mmol dm^{-3} [Ru(NH$_3$)$_6$]$^{3+/2+}$ and (c) 0.5 mmol dm^{-3} [Fe(CN)$_6$]$^{4-/3-}$ in 0.1 mol dm^{-3} NaNO$_3$ at various scan rates (2, 5, 10, 20, 50 and 100 mV s^{-1} for the [FcMeOH] and [Ru(NH$_3$)$_6$]$^{3+/2+}$ redox species and 2, 5, 10 and 20 mV s^{-1} for the [Fe(CN)$_6$]$^{4-/3-}$ redox couple); reliance of peak current as a function of square root of scan rates for the film containing C$_{22}$TAB deposited at -1.25 V (vs. Ag/AgCl) for 20 s on an ITO electrode. All experiments were carried out after surfactant removal: (d) [FcMeOH], (e) [Ru(NH$_3$)$_6$]$^{3+/2+}$ and (f) [Fe(CN)$_6$]$^{4-/3-}$.

The RS equation may be modified to take account of the proportion of the surface that is accessible to the electrolyte by including a porosity parameter as shown in eq 7.[48] Porosity (φ) values calculated from the pore spacing and pore diameter measurements were in the range between 0.1 and 0.7 (supplementary information, Table S1). The apparent diffusion coefficients calculated from the gradient of the linear plots, and assuming that the concentrations of the redox species in the film are the same as those in the bulk solution, are given in Table 1 together with the surfactants and the active species. The apparent diffusion coefficient increases with the size of surfactant used to produce the film, providing further evidence of pore expansion and easier electrochemical access through the pores with surfactant chain length. However, it is noted that the silica film will change the concentration of the active species in the pores relative to the bulk solution to some extent. For example, the D values for $[Fe(CN)_6]^{4-/3-}$ species are smaller than for the $[FcMeOH]$ and $[Ru(NH_3)_6]^{3+/2+}$ species due to the Gibbs-Donnan effect mentioned earlier.

$$i_p = (2.69 \times 10^5)\, n^{3/2}\, \varphi A C D^{1/2}\, v^{1/2} \qquad \text{Eq 7}$$

Table 1. Apparent diffusion coefficients of EASA films with surfactants of increasing chain length using a range of redox active probes.

Surfactant	$D_{[FcMeOH]}$	$D_{[Ru(NH3)6]3+/2+}$	$D_{[Fe(CN)6]4-/3-}$
$C_{14}TAB$	7.4×10^{-7} cm^2 s^{-1}	6.8×10^{-7} cm^2 s^{-1}	1.4×10^{-7} cm^2 s^{-1}
$C_{16}TAB$	8.9×10^{-7} cm^2 s^{-1}	8.2×10^{-7} cm^2 s^{-1}	2.8×10^{-7} cm^2 s^{-1}
$C_{18}TAB$	9.4×10^{-7} cm^2 s^{-1}	1.1×10^{-6} cm^2 s^{-1}	3.8×10^{-7} cm^2 s^{-1}
$C_{20}TAB$	2.3×10^{-6} cm^2 s^{-1}	2.2×10^{-6} cm^2 s^{-1}	5.2×10^{-7} cm^2 s^{-1}
$C_{22}TAB$	4.6×10^{-6} cm^2 s^{-1}	3.5×10^{-6} cm^2 s^{-1}	8.6×10^{-7} cm^2 s^{-1}

Conclusions

Ordered mesoporous silica films with vertically aligned pores were produced by an electrochemically driven sol-gel method (EASA). Pore size was increased by extending the alkyl chain length in the $[Me_3NR]Br$ surfactant from 16 to 22 carbons using quaternary ammonium salts which resulted in larger pore diameters, together with retained order. The film became disordered when adding $C_{24}TAB$ into the sol electrolyte, indicating a constraint in response to micelle expansion using linear chained surfactants, although the vertical pore orientation was retained. The ion diffusion rates using redox active probes were found to increase with surfactant size and hence pore size. The pore size increased from 2.8 nm using $C_{16}TAB$ to 4.4 nm using $C_{22}TAB$. The expanded pores in these

vertically aligned mesoporous silica films may make them more amenable to use as templates for electrochemical deposition of nanowires, and change their behavior in sensing applications.

Notes

The authors affirm that there are no conflicts of interest.

Supporting Information. NMR and mass spectra; further GISAXS data; cyclic voltammograms and diffusion coefficient calculations; tabulated pore spacing and porosity data.

Acknowledgements

References

(1) Li, C.; Iqbal, M.; Lin, J.; Luo, X.; Jiang, B.; Malgras, V.; Wu, K. C. W.; Kim, J.; Yamauchi, Y. Electrochemical Deposition: An Advanced Approach for Templated Synthesis of Nanoporous Metal Architectures. *Acc. Chem. Res.* **2018**, *51* (8), 1764–1773. https://doi.org/10.1021/acs.accounts.8b00119.

(2) Hao, J.; Yang, Y.; Zhao, J.; Liu, X.; Endres, F.; Chi, C.; Wang, B.; Liu, X.; Li, Y. Ionic Liquid Electrodeposition of Strain-Released Germanium Nanowires as Stable Anodes for Lithium Ion Batteries. *Nanoscale* **2017**, *9* (24), 8481–8488. https://doi.org/10.1039/c7nr00264e.

(3) Kim, H.; Cho, J. Hard Templating Synthesis of Mesoporous and Nanowire SnO_2 Lithium Battery Anode Materials. *J. Mater. Chem.* **2008**, *18* (7), 771–775. https://doi.org/10.1039/b714904b.

(4) Tan, M.; Hao, Y.; Deng, Y.; Yan, D.; Wu, Z. Tilt-Structure and High-Performance of Hierarchical $Bi_{1.5}Sb_{0.5}Te_3$ Nanopillar Arrays. *Sci. Rep.* **2018**, *8* (1), 1–9. https://doi.org/10.1038/s41598-018-24872-4.

(5) Xu, Y.; Ding, Q.; Li, L.; Xie, Z.; Jiang, G. Facile Fabrication of Porous Co_3O_4 Nanowires for High Performance Supercapacitors. *New J. Chem.* **2018**, *42* (24), 20069–20073. https://doi.org/10.1039/c8nj05171b.

(6)   Kanno, Y.; Suzuki, T.; Yamauchi, Y.; Kuroda, K. Preparation of Au Nanowire Films by Electrodeposition Using Mesoporous Silica Films as a Template: Vital Effect of Vertically Oriented Mesopores on a Substrate. *J. Phys. Chem. C* **2012**, *116* (46), 24672–24680. https://doi.org/10.1021/jp308772b.

(7)   Wu, C. W.; Yamauchi, Y.; Ohsuna, T.; Kuroda, K. Structural Study of Highly Ordered Mesoporous Silica Thin Films and Replicated Pt Nanowires by High-Resolution Scanning Electron Microscopy (HRSEM). *J. Mater. Chem.* **2006**, *16* (30), 3091–3098. https://doi.org/10.1039/b604062d.

(8)   Bartlett, P. N.; Beanland, R.; Burt, J.; Hasan, M. M.; Hector, A. L.; Kashtiban, R. J.; Levason, W.; Lodge, A. W.; Marks, S.; Naik, J.; Rind, A.; Reid, G.; Richardson, P. W.; Sloan, J.; Smith, D. C. Exploration of the Smallest Diameter Tin Nanowires Achievable with Electrodeposition: Sub 7 Nm Sn Nanowires Produced by Electrodeposition from a Supercritical Fluid. *Nano Lett.* **2018**, *18* (2), 941–947. https://doi.org/10.1021/acs.nanolett.7b04330.

(9)   Xu, J.; Zhang, W.; Morris, M. A.; Holmes, J. D. The Formation of Ordered Bismuth Nanowire Arrays within Mesoporous Silica Templates. *Mater. Chem. Phys.* **2007**, *104* (1), 50–55. https://doi.org/10.1016/j.matchemphys.2007.02.043.

(10)   Nasir, T.; Zhang, L.; Vilà, N.; Herzog, G.; Walcarius, A. Electrografting of 3-Aminopropyltriethoxysilane on a Glassy Carbon Electrode for the Improved Adhesion of Vertically Oriented Mesoporous Silica Thin Films. *Langmuir* **2016**, *32* (17), 4323–4332. https://doi.org/10.1021/acs.langmuir.6b00798.

(11)   Rohlfing, D. F.; Rathouský, J.; Rohlfing, Y.; Bartels, O.; Wark, M. Functionalized Mesoporous Silica Films as a Matrix for Anchoring Electrochemically Active Guests. *Langmuir* **2005**, *21* (24), 11320–11329. https://doi.org/10.1021/la051616a.

(12)   Etienne, M.; Grosso, D.; Boissière, C.; Sanchez, C.; Walcarius, A. Electrochemical Evidences of Morphological Transformation in Ordered Mesoporous Titanium Oxide Thin Films. *Chem. Commun.* **2005**, No. 36, 4566–4568. https://doi.org/10.1039/b508093b.

(13)   Sun, Q.; Yan, F.; Yao, L.; Su, B. Anti-Biofouling Isoporous Silica-Micelle Membrane Enabling Drug Detection in Human Whole Blood. *Anal. Chem.* **2016**, *88* (17), 8364–8368. https://doi.org/10.1021/acs.analchem.6b02091.

(14)   Yan, F.; Zheng, W.; Yao, L.; Su, B. Direct Electrochemical Analysis in Complex Samples Using ITO Electrodes Modified with Permselective Membranes Consisting of Vertically Ordered

Silica Mesochannels and Micelles. *Chem. Commun.* **2015**, *51* (100), 17736–17739. https://doi.org/10.1039/c5cc08425c.

(15)   Nasir, T.; Herzog, G.; Hébrant, M.; Despas, C.; Liu, L.; Walcarius, A. Mesoporous Silica Thin Films for Improved Electrochemical Detection of Paraquat. *ACS Sensors* **2018**, *3* (2), 484–493. https://doi.org/10.1021/acssensors.7b00920.

(16)   Brinker, C. J. Evaporation-Induced Self-Assembly: Functional Nanostructures Made Easy. *MRS Bull.* **2004**, *29* (9), 631–640. https://doi.org/10.1557/mrs2004.183.

(17)   Yan, Y.; King, S. C.; Li, M.; Galy, T.; Marszewski, M.; Kang, J. S.; Pilon, L.; Hu, Y.; Tolbert, S. H. Exploring the Effect of Porous Structure on Thermal Conductivity in Templated Mesoporous Silica Films. *J. Phys. Chem. C* **2019**, *123* (35), 21721–21730. https://doi.org/10.1021/acs.jpcc.9b03767.

(18)   Miyata, H.; Takahashi, M. Lithographically Formed Fine Wavy Surface Morphology for Universal Alignment Control of Mesochannels in Mesostructured Silica Films. *Langmuir* **2021**, *37* (6), 2179–2186. https://doi.org/10.1021/acs.langmuir.0c03494.

(19)   Yamauchi, Y. Field-Induced Alignment Controls of One-Dimensional Mesochannels in Mesoporous Materials. *Nippon Seramikkusu Kyokai Gakujutsu Ronbunshi/Journal Ceram. Soc. Japan* **2013**, *121* (1417), 831–840. https://doi.org/10.2109/jcersj2.121.831.

(20)   Richman, E. K.; Brezesinski, T.; Tolbert, S. H. Vertically Oriented Hexagonal Mesoporousfilms Formed through Nanometre-Scaleepitaxy. *Nat. Mater.* **2008**, *7* (9), 712–717. https://doi.org/10.1038/nmat2257.

(21)   Otomo, J.; Wang, S.; Takahashi, H.; Nagamoto, H. Microstructure Development of Mesoporous Silica Thin Films with Pore Channels Aligned Perpendicularly to Electrode Surfaces and Application to Proton Conducting Composite Electrolyte Membranes. *J. Memb. Sci.* **2006**, *279* (1–2), 256–265. https://doi.org/10.1016/j.memsci.2005.12.013.

(22)   Yamauchi, Y.; Sawada, M.; Sugiyama, A.; Osaka, T.; Sakka, Y.; Kuroda, K. Magnetically Induced Orientation of Mesochannels in 2D-Hexagonal Mesoporous Silica Films. *J. Mater. Chem.* **2006**, *16* (37), 3693–3700. https://doi.org/10.1039/b608780a.

(23)   Otomo, J.; Kurokawa, R.; Takahashi, H.; Nagamoto, H. Kinetic Process of Phase Separation in Co-SiO2 Thin Films and Preparation of Mesoporous SiO2 Thin Films with Mesopore Channels Aligned Perpendicularly to Substrate Surfaces. *Vacuum* **2007**, *81* (8), 1003–1011. https://doi.org/10.1016/j.vacuum.2006.12.007.

(24)   Teng, Z.; Zheng, G.; Dou, Y.; Li, W.; Mou, C. Y.; Zhang, X.; Asiri, A. M.; Zhao, D. Highly Ordered Mesoporous Silica Films with Perpendicular Mesochannels by a Simple Stöber-Solution Growth Approach. *Angew. Chemie - Int. Ed.* **2012**, *51* (9), 2173–2177. https://doi.org/10.1002/anie.201108748.

(25)   Walcarius, A.; Sibottier, E.; Etienne, M.; Ghanbaja, J. Electrochemically Assisted Self-Assembly of Mesoporous Silica Thin Films. *Nat. Mater.* **2007**, *6* (8), 602–608. https://doi.org/10.1038/nmat1951.

(26)   Vilà, N.; André, E.; Ciganda, R.; Ruiz, J.; Astruc, D.; Walcarius, A. Molecular Sieving with Vertically Aligned Mesoporous Silica Films and Electronic Wiring through Isolating Nanochannels. *Chem. Mater.* **2016**, *28* (8), 2511–2514. https://doi.org/10.1021/acs.chemmater.6b00716.

(27)   Robertson, C.; Beanland, R.; Boden, S. A.; Hector, A. L.; Kashtiban, R. J.; Sloan, J.; Smith, D. C.; Walcarius, A. Ordered Mesoporous Silica Films with Pores Oriented Perpendicular to a Titanium Nitride Substrate. *Phys. Chem. Chem. Phys.* **2015**, *17* (6), 4763–4770. https://doi.org/10.1039/c4cp05730a.

(28)   Ullah, W.; Herzog, G.; vila, neus; Walcarius, A. Polyaniline Nanowire Arrays Generated through Oriented Mesoporous Silica Films: Effect of Pore Size and Spectroelectrochemical Response. *Faraday Discuss.* **2021**. https://doi.org/10.1039/d1fd00034a.

(29)   Scheraga, H. A.; Backus, J. K. Flow Birefringence in Solutions of N-Hexadecyltrimethylammonium Bromide. *J. Am. Chem. Soc.* **1951**, *73* (11), 5108–5112. https://doi.org/10.1021/ja01155a027.

(30)   Al Dulayymi, J. R.; Baird, M. S.; Roberts, E. The Synthesis of a Single Enantiomer of a Major α-Mycolic Acid of M. Tuberculosis. *Tetrahedron* **2005**, *61* (50), 11939–11951. https://doi.org/10.1016/j.tet.2005.09.056.

(31)   Goux, A.; Etienne, M.; Aubert, E.; Lecomte, C.; Ghanbaja, J.; Walcarius, A. Oriented Mesoporous Silica Films Obtained by Electro-Assisted Self-Assembly (EASA). *Chem. Mater.* **2009**, *21* (4), 731–741. https://doi.org/10.1021/cm8029664.

(32)   Etienne, M.; Guillemin, Y.; Grosso, D.; Walcarius, A. Electrochemical Approaches for the Fabrication and/or Characterization of Pure and Hybrid Templated Mesoporous Oxide Thin Films: A Review. *Anal. Bioanal. Chem.* **2013**, *405* (5), 1497–1512. https://doi.org/10.1007/s00216-012-6334-7.

(33)   Ding, L.; Su, B. An Electrochemistry Assisted Approach for Fast, Low-Cost and Gram-Scale Synthesis of Mesoporous Silica Nanoparticles. *RSC Adv.* **2015**, *5* (81), 65922–65926. https://doi.org/10.1039/c5ra13482j.

(34)   Kruk, M.; Jaroniec, M.; Ko, C. H.; Ryoo, R. Characterization of the Porous Structure of SBA-15. *Chem. Mater.* **2000**, *12* (7), 1961–1968. https://doi.org/10.1021/cm000164e.

(35)   Wang, Z.; Chen, B.; Quan, G.; Li, F.; Wu, Q.; Dian, L.; Dong, Y.; Li, G.; Wu, C. Increasing the Oral Bioavailability of Poorly Water-Soluble Carbamazepine Using Immediate-Release Pellets Supported on SBA-15 Mesoporous Silica. *Int. J. Nanomedicine* **2012**, *7* (November), 5807–5818. https://doi.org/10.2147/IJN.S37650.

(36)   Beck, J. S.; Vartuli, J. C.; Roth, W. J.; Leonowicz, M. E.; Kresge, C. T.; Schmitt, K. D.; Chu, C. T. W.; Olson, D. H.; Sheppard, E. W.; McCullen, S. B.; Higgins, J. B.; Schlenker, J. L. A New Family of Mesoporous Molecular Sieves Prepared with Liquid Crystal Templates. *J. Am. Chem. Soc.* **1992**, *114* (27), 10834–10843. https://doi.org/10.1021/ja00053a020.

(37)   Kruk, M.; Jaroniec, M.; Kim, J. M.; Ryoo, R. Characterization of Highly Ordered MCM-41 Silicas Using X-Ray Diffraction and Nitrogen Adsorption. *Langmuir* **1999**, *15* (16), 5279–5284. https://doi.org/10.1021/la990179v.

(38)   A. J. Bard and L. R. Faulkner. *Electrochemical Methods: Fundamentals and Applications*; Wiley: New York, 1980.

(39)   Baklanov, M. R.; Mogilnikov, K. P.; Polovinkin, V. G.; Dultsev, F. N. Determination of Pore Size Distribution in Thin Films by Ellipsometric Porosimetry. *J. Vac. Sci. Technol. B Microelectron. Nanom. Struct.* **2000**, *18* (3), 1385. https://doi.org/10.1116/1.591390.

(40)   Baklanov, M. R.; Mogilnikov, K. P. Non-Destructive Characterisation of Porous Low-k Dielectric Films. *Microelectron. Eng.* **2002**, *64* (1–4), 335–349. https://doi.org/10.1016/S0167-9317(02)00807-9.

(41)   Robertson, C.; Lodge, A. W.; Basa, P.; Carravetta, M.; Hector, A. L.; Kashtiban, R. J.; Sloan, J.; Smith, D. C.; Spencer, J.; Walcarius, A. Surface Modification and Porosimetry of Vertically Aligned Hexagonal Mesoporous Silica Films. *RSC Adv.* **2016**, *6* (114), 113432–113441. https://doi.org/10.1039/c6ra23059h.

(42)   Thommes, M.; Kaneko, K.; Neimark, A. V.; Olivier, J. P.; Rodriguez-Reinoso, F.; Rouquerol, J.; Sing, K. S. W. Physisorption of Gases, with Special Reference to the Evaluation of Surface Area and Pore Size Distribution (IUPAC Technical Report). *Pure Appl. Chem.* **2015**, *87* (9–10), 1051–

1069. https://doi.org/10.1515/pac-2014-1117.

(43)   Jahandar Lashaki, M.; Fayaz, M.; Niknaddaf, S.; Hashisho, Z. Effect of the Adsorbate Kinetic
         Diameter on the Accuracy of the Dubinin-Radushkevich Equation for Modeling Adsorption of
         Organic Vapors on Activated Carbon. *J. Hazard. Mater.* **2012**, *241–242*, 154–163.
         https://doi.org/10.1016/j.jhazmat.2012.09.024.

(44)   Shimizu, W.; Hokka, J.; Sato, T.; Usami, H.; Murakami, Y. Microstructure Investigation on
         Micropore Formation in Microporous Silica Materials Prepared via a Catalytic Sol-Gel Process
         by Small Angle X-Ray Scattering. *J. Phys. Chem. B* **2011**, *115* (30), 9369–9378.
         https://doi.org/10.1021/jp203385y.

(45)   Calleja, G. .; Serrano, D. P. .; Botas, J. A. .; Gutierrez, F. J. . Adsorption Properties of MCM-41
         Materials for the VOCs Abatement. *Stud. Surf. Sci. Catal.* **2002**, *142*, 1671–1678.

(46)   Karman, C.; Vilà, N.; Walcarius, A. Amplified Charge Transfer for Anionic Redox Probes
         through Oriented Mesoporous Silica Thin Films. *ChemElectroChem* **2016**, *3* (12), 2130–2137.
         https://doi.org/10.1002/celc.201600303.

(47)   Etienne, M.; Quach, A.; Grosso, D.; Nicole, L.; Sanchez, C.; Walcarius, A. Molecular Transport
         into Mesostructured Silica Thin Films: Electrochemical Monitoring and Comparison between
         P6m, P63//WWIC, and Pm3n Structures. *Chem. Mater.* **2007**, *19* (4), 844–856.
         https://doi.org/10.1021/cm0625068.

(48)   Platt, M.; Dryfe, R. A. W.; Roberts, E. P. L. Voltammetry with Liquid/Liquid Microarrays:
         Characterization of Membrane Materials. *Langmuir* **2003**, *19* (19), 8019–8025.
         https://doi.org/10.1021/la034726v.